



HHS Public Access

Author manuscript

Contemp Phys. Author manuscript; available in PMC 2024 March 08.

Published in final edited form as:

Contemp Phys. 2022 ; 63(3): 161–179. doi:10.1080/00107514.2023.2182950.

Quantum enabled functional neuroimaging: the why and how of magnetoencephalography using optically pumped magnetometers

Holly Schofield^{a,b}, Elena Boto^{b,a}, Vishal Shah^c, Ryan M. Hill^{a,b}, James Osborne^c, Molly Rea^{b,a}, Cody Doyle^c, Niall Holmes^{a,b}, Richard Bowtell^a, David Woolger^b, Matthew J. Brookes^{a,b}

^aSir Peter Mansfield Imaging Centre, School of Physics and Astronomy, University of Nottingham, Nottingham, UK;

^bCerca Magnetics Limited, Nottingham, UK;

^cQuSpin Inc., Louisville, CO, USA

Abstract

Non-invasive imaging has transformed neuroscientific discovery and clinical practice, providing a non-invasive window into the human brain. However, whilst techniques like MRI generate ever more precise images of brain structure, in many cases, it's the *function* within neural networks that underlies disease. Here, we review the potential for quantum-enabled magnetic field sensors to shed light on such activity. Specifically, we describe how optically pumped magnetometers (OPMs) enable magnetoencephalographic (MEG) recordings with higher accuracy and improved practicality compared to the current state-of-the-art. The paper is split into two parts: first, we describe the work to date on OPM-MEG, detailing *why* this novel biomagnetic imaging technique is proving disruptive. Second, we explain *how* fundamental physics, including quantum mechanics and electromagnetism, underpins this developing technology. We conclude with a look to the future, outlining the potential for OPM-MEG to initiate a step change in the understanding and management of brain health.

Keywords

Magnetoencephalography; brain imaging; optically pumped magnetometer

1. Functional neuroimaging

Around 1 in 4 people will suffer a mental health condition at some point in their life; 1 person is admitted to a UK hospital every 90s with concussion; 65 million people in the world suffer from epilepsy; 55 million people suffer from dementia. These statistics

Disclosure statement

V.S. is the founding director of QuSpin, the commercial entity selling OPM magnetometers. J.O. and C.D. are employees of QuSpin. E.B., M.J.B. and D.W. are directors of Cerca Magnetics Limited, a spin-out company whose aim is to commercialise aspects of OPM-MEG technology. E.B., M.J.B., D.W., R.B., N.H. and R.M.H. hold founding equity in Cerca Magnetics Limited. H.S. and M.R. are employees of Cerca Magnetics Limited.

demonstrate that the human brain and the disorders that affect it represent a major challenge for twenty-first century healthcare. In the latter part of the twentieth century, the advent of human imaging – underpinned by fundamental physics – revolutionised healthcare by providing a non-invasive window on the body. Techniques like magnetic resonance imaging (MRI) [1] and X-ray CT [2], now enable visualisation of brain anatomy with sub-millimetre precision. Such techniques are commonplace, and paramount not only for diagnosis but our understanding of disease. However, in many disorders the brain “looks” normal – with no structural deficits. In other cases, structural abnormalities are found, but it’s unclear which, if any, drive disease. In these cases, it proves useful to move beyond structure, and towards measurements of brain function.

Characterising brain function introduces two significant challenges. First, we must find a means to measure “activity” in a network of ~ 100 billion neurons. Second, this measurement must be made in an environment where it is possible to evoke brain function in a naturalistic way. The ‘gold standard’ is intracranial electroencephalography (iEEG), where electrodes are placed on or beneath the brain surface [3]. iEEG enables measurement of electrical activity that mediates brain function, across multiple spatial scales with high temporal resolution. Although iEEG involves major surgery, once patients have devices implanted it is possible to conduct experiments that elicit natural brain activity. However, iEEG is highly invasive and can only be used in patient populations who benefit from the procedure. Electrode grids lack whole brain coverage (i.e. you can’t place electrodes everywhere) and are (by definition) placed close to abnormal tissue making the study of healthy brain function challenging.

Perhaps the most widespread non-invasive measurement of brain activity is functional Magnetic Resonance Imaging (fMRI), which exploits the para-/dia-magnetic properties of deoxy-/oxy-haemoglobin as an endogenous contrast agent, known as the Blood Oxygen Level Dependent (BOLD) response [4]. BOLD can be used to map areas of increased metabolic demand during a task, with excellent spatial resolution (< 1 mm resolution can be achieved at very high magnetic fields) and has proved a disruptive tool in the field of cognitive neuroscience. However, the haemodynamic response peaks about 5–6 s after the onset of a neural response, meaning fMRI has poor temporal resolution and cannot directly measure electrophysiological signals. The constrained environment of an MRI scanner makes it hard to evoke activity in a natural way and many vulnerable cohorts find the MR environment challenging (whilst sedation is possible for structural scanning, it is not an option for measures of brain function). In addition to fMRI, similar “indirect” haemodynamic responses are measurable via Positron Emission Tomography (PET) [5] and functional Near Infra-Red Spectroscopy (fNIRS) [6]; PET has similar limitations to fMRI for functional measurement in terms of scanning environment, with the added disadvantage that it requires ionising radiation. ANIRS is non-invasive and wearable technology, enabling easy adoption in any cohort and naturalistic tasks. However, it remains a haemodynamic metric, with poor temporal resolution and limited spatial resolution compared to fMRI.

“Direct” and non-invasive measures of electrophysiological activity are possible via scalp-based EEG [7] and magnetoencephalography (MEG) [8]. The electrical currents in neural networks generate both electric and magnetic fields; the former result in measurable changes

in electrical potential at the scalp surface (EEG), whilst the latter pass through the skull and can be measured above the scalp surface (MEG). Both offer unique insights into brain electrophysiology, with extremely high temporal resolution. EEG – first demonstrated nearly a century ago [7] – is a ubiquitous tool for neurophysiological assessment with a broad range of research and clinical applications. Systems are wearable (like fNIRS) enabling experimentation in a naturalistic setting. However, the electrical signals must pass through the inhomogeneous conductivity profile of the head, including the skull which has high resistance. This reduces signal amplitude and spatially distorts the signals, leading to poor spatial resolution. By contrast, the magnetic fields measured by MEG pass through the skull relatively undisturbed, and so MEG offers significantly improved spatial resolution compared to EEG. In addition, whilst fields are small (of order 10^{-15} T), when carried out inside a magnetically shielded room (MSR) MEG offers similar or better sensitivity than EEG. Thus, with direct access to electrophysiology, a spatial resolution of 2–3 mm and temporal resolution of ~ 1 ms, MEG is arguably the best candidate for functional brain imaging. However, the superconducting quantum interference devices (SQUIDs) that are used for signal detection need cryogenic cooling to operate. This requires regularly filling systems with liquid helium (a non-renewable resource), or the use of a liquefier, which are both costly. Moreover, the extremely low temperature required by SQUIDs means that a thermally insulating gap of ~ 2 cm must be maintained between the sensors and scalp. Since magnetic field from the brain diminishes as $1/\text{distance}^2$, this places an upper limit on the strength of the detectable magnetic fields. This upper limit is rarely achieved since heads don't fit the MEG helmet perfectly, resulting in inhomogeneous coverage depending on head shape and location in the MEG helmet. Patients with smaller heads (especially children) are especially difficult to scan. The fixed nature of the superconducting sensors also means that participants must remain still relative to the sensors for the duration of the scan. This makes naturalistic experimentation difficult, rules out some patient cohorts (e.g. those with movement disorders) and makes scanning children challenging.

In summary, whilst viable options for functional neuroimaging exist (see also Figure 1) they suffer limitations in either performance, practicality, or both. However, in recent years, the advancement and commercialisation of quantum sensors has allowed a new functional imaging technique to emerge. OPM-MEG uses optically pumped magnetometers (OPMs) – a highly sensitive magnetometer that does not require cryogenic cooling – to measure the MEG signal. OPMs can be placed closer to the scalp than conventional (SQUID-based) sensors, improving signal strength and spatial precision. Because OPMs are small and lightweight, they can be mounted into a wearable device that is adaptable to individual head sizes – ensuring lifespan compliance. Wearability also allows for motion during scanning, facilitating a more naturalistic scanning environment. It follows that OPM-MEG may offer the best of all worlds: i.e. the practicality of EEG or fNIRS, and performance better than even the most advanced MEG scanners. In this review, we introduce OPM-MEG and the work undertaken to date to develop and use this nascent technology. The review is split into two parts; first, we answer the question *why should OPM-MEG be considered the technique of choice for non-invasive functional neuroimaging?* Second, we introduce the fundamental physics underlying the technique, addressing the question *how does an OPM-MEG instrument work?*

2. Why OPM-MEG?

OPMs rely on the quantum properties of alkali atoms to measure magnetic field. Whilst the physics will be covered later, briefly, an OPM contains a glass cell enclosing an atomic vapour. Each atom possesses a magnetic moment, and manipulation via a laser tuned to a specific transition between quantum states (optical pumping) aligns these magnetic moments, giving the vapour a bulk magnetisation. An understanding of this bulk magnetisation, and its interaction with local magnetic field, allows us to interrogate the atoms in such a way that the local field can be measured in any orientation perpendicular to the direction of the laser beam. The use of multiple beams within a single OPM allows knowledge of the complete 3D field. Sensitivity is of order $15\text{fT}/(\text{Hz})$ – comparable to a SQUID – however dynamic range is limited to $\sim 1.5\text{nT}$.

2.1. Measurement of the neuromagnetic field

OPMs were first used for MEG signal detection in 2006, to measure an auditory evoked response [10]. However, the initial size and weight was a limiting factor for use in mapping brain activity since only a small number of sensors could fit around the head. Subsequent years saw a significant effort to miniaturise the sensors and by 2013 an auditory evoked response had been recorded using a multi-sensor array [11]. There followed efforts towards microfabrication which led to a step change, in 2016, when the first commercial OPMs were made available by QuSpin Inc., catalysing progress by allowing neuroimaging research groups to begin building OPM-MEG systems. Many studies have demonstrated the successful detection of electrophysiological activity (see Figure 2), e.g. in the auditory [11–15], somatosensory [12,16,17] and visual [18] areas. Activity has been measured across the frequency range occupied by most of the key electrophysiological signals, including theta (4–8 Hz) [19] alpha (8–13 Hz) [20], beta (13–30 Hz) [21,22], gamma (30–80 Hz) [23,24] and even very low frequency oscillations (< 4 Hz) [25]. Recent studies have measured functional connectivity with OPMs, demonstrating a fidelity similar to conventional MEG systems [26].

Commercial OPMs are now approximately the size of a Lego brick and weigh ~ 7 g, meaning it is possible to construct high density arrays of sensors mounted flexibly on the scalp surface (see Figure 3) [23,27,28]. In terms of signal measurement, there are two major advantages of OPMs over SQUIDs. First, because they don't require cryogenic cooling, the sensors are able to get closer to the brain; second, unlike SQUIDs which typically only measure the radial component of magnetic field, OPMs can be designed to measure the full field vector.

2.2. Sensor proximity

Sensor proximity is important due to the inverse square law and simulations suggest that scalp-based measurement offers 4–5 times higher signal strength from most cortical sources, compared to SQUID based measurements [29,30]. This is advantageous since most people's heads don't fit a conventional MEG system perfectly; leading to inhomogeneous coverage. Moreover, individuals with smaller heads (e.g. children) are physically further from the sensors giving either very poor signal everywhere, or reasonable signal within a single brain

area. Thus, the ability to mount OPMs directly on the scalp surface, providing the best possible coverage everywhere in the brain, is a major advantage. This said, at the time of writing, the noise floor of an OPM remains higher than that of a SQUID ($\sim 10\text{--}15 \text{ fT/ (Hz)}$) compared to $\sim 5 \text{ fT/ (Hz)}$) which means that the increased signal doesn't translate directly into SNR. In addition, the improvement in signal strength with sensor proximity declines with depth, meaning that whilst one expects a 4–5 fold improvement for (shallow) cortical sources, this becomes less (e.g. $\sim 2\text{-fold}$) in deeper brain areas (e.g. Hippocampus). This coupled with the increased sensor noise means that OPMs, at least for now, don't offer improvements in SNR for all brain regions. Nevertheless, there is evidence [16] that – even in adults – the SNR of OPMs is improved over SQUIDs for cortical sources. Despite this, recent work suggests that despite lower signal, OPMs systems can detect deep sources including hippocampus [31,32] and the cerebellum [33].

Sensor proximity also impacts spatial resolution. As sensors get closer to the brain, field topographies become more 'focal', meaning that the topographies from two separate but nearby sources in the brain become less correlated. This is advantageous when assessing spatial resolution; recent simulations have demonstrated that the theoretical limit on spatial resolution is fundamentally improved for OPM-MEG compared to both conventional MEG and EEG [34]. Further simulations [35] using a densely packed sensor array over a limited patch of scalp (a technique dubbed magnetocorticography (MCoG)) have shown that the array can resolve sources with far greater precision than is possible with conventional MEG and that the technique may even rival (in terms of spatial resolution) iEEG for very shallow cortical sources. These (theoretical) demonstrations highlight the promise of OPM-MEG for high precision brain mapping. Clinically, this could be important; for example, in around a third of epilepsy cases, the disorder is not well controlled by drugs and patients become candidates for surgery, where the brain area responsible for seizure generation is resected. Determining the location of epileptogenic cortex is challenging; structural imaging doesn't always find abnormalities, and when it does, it's not always clear which abnormality drives symptoms. EEG can measure electrophysiological manifestations of epilepsy but lacks the spatial resolution to pinpoint their origin. In adults, a conventional MEG scan is valuable [36] but is costly and difficult to deploy in infants. iEEG remains the gold standard but is highly invasive. With improved spatial specificity compared to conventional MEG, and performance potentially even rivalling iEEG, OPM-MEG could be disruptive in this area. However, at the time of writing there have been no experimental demonstrations quantifying the spatial resolution of OPM-MEG – this will undoubtedly be a future focus.

2.3. Triaxial sensing

Measurement of the full magnetic field vector using a single sensor is made possible by using two perpendicular laser beams. Briefly, assuming a cartesian coordinate system, a laser oriented in the z-direction offers field measurement in x and y; a second beam oriented in x offers field measurement in y and z. Combining measurements provides vector (triaxial) field characterisation, with two measurements in y which are averaged. However, using two beams necessitates beam splitting, reducing the effective power of each beam (which in principle has detrimental effects on sensor noise). Nevertheless, this has been realised [37] and early demonstrations [38] showed a noise floor of 13.5 fT/ (Hz) and 14.9 fT/ (Hz) in the x

and z orientations respectively with $9.9\text{fT}/\text{Hz}$ in y – marginally higher than single axis sensors (which are typically $13.8\text{fT}/\text{Hz}$) in z but nevertheless viable for MEG recording.

The advantages provided by triaxial measurement require some explanation. Assuming a spherical conductor model, if one has perfect knowledge of the radial field everywhere across a sphere surface, then the tangentially oriented fields can be calculated directly from the radial field and Maxwell equations [39] – meaning that in theory, tangential field measurement offers no new “information” on the fields from the brain compared to radial only fields. However, finite spatial sampling means we don’t know the field everywhere, measurements are corrupted by sensor noise, and external fields (interference) impinge on the instrumentation. Given these considerations, there are 3 reasons why triaxial measurement is helpful: First, the total amount of signal from the brain is increased approximately twofold (one might expect threefold, but the tangential signal components are smaller than the radial [27,40]). This enables a greater degree of signal averaging which reduces sensor noise and improves SNR. Second, when the number of sensors is limited triaxial measurement improves the homogeneity of coverage of shallow cortical sources (this is particularly important for paediatric measurements [38]). Finally, we gain more information on the spatial topography of interference fields. This leads to an improvement in the ability to eliminate fields of no interest [27,40]. In addition, from a technical point of view, triaxial sensors eliminate the problem of sensors being affected by other sensors in close proximity and allow unambiguous closed loop operation (see Section 3).

Triaxial sensors have only recently become available, nevertheless they have been used successfully. Rea et al. [27] used a 30 sensor (90 channel) array to measure brain networks during a handwriting task. Rier et al. [41] used a 168 channel triaxial array to demonstrate a high degree of test-retest reliability of connectivity measurement in individuals watching a movie. These studies are some of the first to suggest that MEG with triaxial sensing is not only viable, but perhaps the best design of OPM-MEG system.

2.4. Wearability, lifespan compliance and beyond the brain

The compact and lightweight nature of OPMs allow them to be mounted on the head. Furthermore, the sensors move with the head, enabling naturalistic movement during scanning. This offers opportunities for novel types of neuroscientific experimentation, including new cohorts (e.g. infants) and paradigms in which participants can undertake large scale movement. However, the realisation of this is a significant technical challenge.

2.5. Natural movement

OPMs are directionally sensitive field sensors, and this is critical to enable the generation of functional images from field data. However, if an OPM either rotates in a spatially uniform background field, or translates in a field gradient, it will “see” (hence measure) a magnetic field that appears to change in time. This brings about significant technical challenges relating to both high amplitude interference (i.e. the changing field observed by the OPMs will obfuscate fields from the brain) and dynamic range (the field change due to movement is, in some instances, large enough to take an OPM outside its operational range). For these reasons a “wearable” (i.e. moves with the head) OPM-MEG system is only viable with

stringent restrictions on local magnetic field. Specifically, background field must be reduced to $< 1\text{nT}$ to enable system operation [21,42,43]. There are two ways to shield a system against external field; passive shielding is a technique in which measurements are carried out in a space surrounded by multiple layers of high permeability and high conductivity material (i.e. within a MSR). Active shielding is the process of measuring local magnetic field and then using electromagnetic coils to generate a field that is equal and opposite to the measurement, thus cancelling the existing field. The physics of such shielding systems will be introduced later, nevertheless the critical point is that a combination of these two techniques have enabled introduction of wearable MEG (for examples see Figure 4).

In an initial demonstration, Boto and colleagues used a 13 channel OPM system in conjunction with a “standard” MSR and bi-planar electromagnetic coils [42] to make measurements of sensorimotor beta band modulation, whilst a (seated) subject made natural movements (including drinking a cup of tea and playing a ball game) [21]. In a follow up paper, an adult participant undertook a retinotopy task in which they were asked to move their head so that a (static) visual stimulus appeared either in the left or right visual hemisphere. Results showed that the response shifted retinotopically in the visual cortex as would be expected [42]. A further study [44] achieved a similar effect but via stimulation using virtual reality. In Rea et. al (2021) [45], the authors used a high precision field mapping technique (in which background field was sampled via movement of the head) to show that background field could be collapsed as low as 0.3 nT. They showed that visual responses could be delineated even in the presence of large and rapid head movement. Whilst compelling, a limitation of bi-planar coils is that field can only be generated in a fixed volume containing the head. Meaning whilst head movement was possible, more expansive motion (e.g. standing up or walking) would take the head outside of the nulled volume.

More expansive types of movement have been attempted. In an initial study, Seymour et al. [46] demonstrated that, in an OPM-optimised shielded room (Cerca Magnetics Limited) OPM-MEG could be used to measure auditory evoked responses in seated, standing and standing/mobile participants, with similar results in each case despite large scale ($\sim 20\text{ cm}$) movements. In Holmes et al. [47], a new type of field control system – the matrix coil – was used to allow a field nulled volume to be placed flexibly in multiple locations within a room, and to follow (in real time) a participant around a room as they undertook a task. This system uses multiple independently controlled coils to correct the background field measured across the sensor array. High-quality MEG source data were collected despite the presence of large (65 cm translations and 270° rotations) ambulatory participant movements. This enables positioning of a participant anywhere within a room. Moreover, a participant could be scanned whilst walking around a room. The demonstration even permits scanning of multiple people at the same time using two separate regions of active field control. Such demonstrations potentially enable new ideas for experimental paradigms, for example it may be possible to measure brain function in a child as they learn to walk, or in a patient with movement disorders as they attempt to perform mobile tasks.

2.6. Lifespan compliance

The accommodation of movement, coupled with the flexibility of sensor placement, has enabled demonstrations that OPM-MEG has lifespan compliance. This field is in its infancy and at the time of writing, whilst there are several ongoing exciting studies, relatively little is published; recent examples are shown in Figure 5.

In an early study, Hill et al. [48] used a 24 sensor wearable system to image somatosensory activity in a 2-year-old, and a 5-year old. Both showed similar data quality to that found in an adult undertaking the same task. In a follow up study, Boto et al. [38] used a similar somatosensory paradigm to successfully induce oscillatory activity in a 6-year-old, who was scanned using a triaxial OPM-MEG array. Recent work by Feys et al. [49] used a 32 sensor OPM-MEG array to measure inter-ictal epileptic events in a group of children in the 5-to-11-year age range. Results were compared directly to SQUID based measurements in the same individuals. Results not only showed that interictal spikes could be clearly detected using wearable OPM-MEG, but further that OPM-MEG demonstrated significantly higher SNR when compared to conventional MEG. Perhaps most significantly, studies have been carried out in which epileptic participants were scanned during a seizure [50,51]. In Feys et al. [51], the participant was a 10 -year-old male. Source localisation of the resulting data showed that the seizure onset zone could be localised. The results of these epilepsy studies (shown in Figure 5B) capture the clinical potential of MEG, combining lifespan compliance with motion robustness and high spatio-temporal resolution.

2.7. Beyond the brain

Finally, the potential for use of OPMs to capture electrophysiological effects from areas of the body outside the brain should be highlighted. The heart, muscles, spine, and gut all generate electrical signals which are detectable via OPM sensors. In addition, OPM arrays placed around abdomen during pregnancy have been proven to enable foetal cardiac monitoring [52]. Of particular excitement is the idea that sensors can be placed both over the brain and peripheral areas – for example a recent study [53] showed that it was uniquely possible to capture electrophysiological interactions between the brain and spine using a single system with OPMs split across regions. Each of these areas is expanding rapidly and it is not our intention to cover each in detail here – indeed each warrants a review paper in its own right. However, the salient point is that whether scanning the heart, spine, muscles, foetus, or brain, the same OPMs can be used, just mounted in a different way. This is distinct from superconducting (SQUID) technology in which multiple costly systems would be required for each application. From a commercial standpoint this means that an OPM-MEG system, which is already cheaper to purchase and run than a conventional SQUID based system, can be used for more than just functional brain imaging.

3. How does OPM-MEG work?

OPM-MEG is rooted in fundamental physics including quantum mechanics, which enables the sensor to operate and electromagnetism which explains both the signal that we detect and the generation of an environment in which we can detect it. In this section, we outline the fundamental concepts underlying both of these areas.

3.1. Quantum mechanics of an OPM

The OPM sensor head (shown schematically in Figure 6A,B) comprises a laser, a glass cell containing a high-pressure vapour of alkali atoms (such as ^{87}Rb), a photodiode and a set of on-board electromagnetic coils to control field within the cell.

Optical pumping refers to the preparation of the atoms in into a single quantum state through the application of laser light. Alkali atoms are good candidates for optical pumping, since they have one unpaired electron in their outermost shell which can be easily manipulated. The applied laser light delivers not only energy, but also angular momentum to the atoms, driving transitions between quantum states.

To explain this process, it is first necessary to recap atomic angular momentum and structure. The angular momentum of an atom, \mathbf{F} , is given by the sum of the angular momentum of the electron, \mathbf{J} , and nucleus, \mathbf{I} such that,

$$\mathbf{F} = \mathbf{J} + \mathbf{I}. \quad (1)$$

This angular momentum determines the atomic magnetic moment, μ_F , thus

$$\mu_F = \gamma \mathbf{F}, \quad (2)$$

where γ is the gyromagnetic ratio. (For ^{87}Rb , $\gamma \sim 28 \text{ Hz/nT}$ and $I = 3/2$) [54]. The angular momentum of the electron can be further split into its orbital angular momentum, \mathbf{L} , and its spin, \mathbf{S} , such that

$$\mathbf{J} = \mathbf{L} + \mathbf{S}, \quad (3)$$

where $S = 1/2$ for electrons. The orbital angular momentum, \mathbf{L} , depends on the energy level that the electron occupies. When it occupies the ground state, the single outermost electron in an alkali metal has $L = 0$. When it occupies the first excited state, $L = 1$. Note that L and S are both dimensionless quantum numbers, which are related to the orbital and spin angular momentum respectively as

$$|\mathbf{L}| = \sqrt{L(L+1)}\hbar, \quad (4)$$

$$|\mathbf{S}| = \sqrt{S(S+1)}\hbar, \quad (5)$$

where \hbar is the reduced Planck's constant ($\frac{h}{2\pi} \sim 1.05 \times 10^{-34}$).

3.2. Atomic energy structure

Interactions between the electron's orbital angular momentum, L , and its spin, S , affect the energy levels occupied by these two states – a phenomenon known as *spin-orbit coupling*. To explain this classically, we consider that the electron is orbiting the nucleus, or (in the rest frame of the electron) the positively charged nucleus orbits the electron, creating a current loop around it. Like any current loop, this gives rise to a magnetic field which the electron experiences. Due to its inherent spin and charge, the electron has its own magnetic moment. The interaction of the two fields causes splitting of the atomic energy levels that is known as *fine structure*. These fine structure energy levels are defined by the quantum number J and are found at integer steps in the range

$$|L - S| \leq J \leq L + S. \quad (6)$$

Therefore, for the ground state there is only one fine structure level at $J = 1/2$, but for the excited state there are two possible levels at $J = 1/2$ and $J = 3/2$. This means there are two possible energy transitions between the ground ($L = 0, J = 1/2$) and the excited states ($L = 1, J = 1/2$) and ($L = 1, J = 3/2$), which are referred to as the D1 and D2 transitions.

It is possible to selectively drive D1 transitions by irradiating the sample with laser light. To achieve this, the energy of the photons must equal the energy difference between the two relevant states. For ^{87}Rb , a laser with a wavelength of 795 nm is required to induce a D1 transition.

Energy levels are further split into pairs (*doublets*) due to interaction between the nuclear magnetic moment, I , and the electron spin, S . This is known as the hyperfine structure, with energy levels defined by the quantum number F and existing in the range

$$|I - J| \leq F \leq I + J. \quad (7)$$

Considering the ground ($L = 0, J = 1/2$) and excited ($L = 1, J = 1/2$) states in ^{87}Rb atoms and remembering $I = 3/2$, both states split into two hyperfine levels with $F = 1$ and $F = 2$.

Finally, in the presence of an external magnetic field, the hyperfine structure is further split into sublevels along a quantisation axis. This is known as Zeeman splitting [55]. The projection of the atomic angular momentum, F , along this quantisation axis is described by another dimensionless quantum number, m_F , for which the allowed values are

$$-F \leq m_F \leq F. \quad (8)$$

In zero magnetic field, the quantisation axis is the direction of the laser beam through the vapour cell. Multiplying m_F by Planck's constant, h , gives the component of angular momentum, F , along this axis of laser propagation. Considering ^{87}Rb again, for the $F = 1$ hyperfine state, $m_F = -1, 0, 1$ and for the $F = 2$ hyperfine state, $m_F = -2, -1, 0, 1, 2$.

The energy difference between the Zeeman sublevels is given by

$$\Delta E = g_F \mu_B B, \quad (9)$$

where g_F is the hyperfine Lande g-factor, μ_B is the Bohr magneton and B is the magnetic field. The electron spin in an external field B precesses at the Larmor frequency

$$\omega = \gamma B, \quad (10)$$

where γ is the gyromagnetic ratio. For the valence electron in ^{87}Rb , this is given as

$$\frac{\gamma_F}{2\pi} = \frac{g_F \mu_B}{\hbar}, \quad (11)$$

where $g_F = -1/2$ for the $F = 1$ state and $g_F = 1/2$ for the $F = 2$ state. This leads to a gyromagnetic ratio of

$$\frac{\gamma_F}{2\pi} = \pm 7 \frac{\text{Hz}}{\text{nT}}, \quad (12)$$

depending on which hyperfine state the atom is in (the nuclear slowing down factor $Q(P) = 4$ (see Maintaining Spin Polarisation with the SERF Regime), reduces γ_F by a factor of 4 from $\sim 28 \text{ Hz/nT}$ to $\sim 7 \text{ Hz/nT}$). Due to the opposite signs of g_F , the two states $F = 1$ and $F = 2$ precess in opposing directions [54].

3.3. Optical pumping

The aim of optical pumping is to drive energy transitions so that as many atoms as possible occupy the same quantum state. In OPMs, this is achieved using circularly polarised light. When light is circularly polarised, photons have the same spin projection along the direction of laser propagation. For light that is right-hand-circularly-polarised, all photons have angular momentum of $+1$ along the propagation direction. When irradiating atoms with a single valence electron, due to conservation of angular momentum the polarised light obeys a selection rule, meaning it can only induce transitions such that

$$\Delta m_F = m_{F, \text{final}} - m_{F, \text{initial}} = +1.$$

(13)

This increase in m_F refers to a transfer of angular momentum from the photon to the atom. Therefore, when a ^{87}Rb atom absorbs a photon, it will not only transition to its excited state ($L = 1, J = 1/2$) but it will also experience an increase in m_F of +1. The atom will eventually return to its ground state ($L = 0, J = 1/2$) through spontaneous emission of a photon, but the emitted photon has an equal chance of causing $\Delta m_F = -1, 0, 1$.

Through continued absorption and emission, the atoms will eventually be driven into the ($F = 2, m_F = 2$) Zeeman sublevel and the $L = 0$ state. At this point, the D1 transition is no longer possible (since it would require a +1 increase in m_F , which is forbidden). Therefore, the laser light passes through the vapour cell unaffected, as no more photons are absorbed by the atoms. This is known as the ‘dark state’ since the atoms become transparent to the laser. With the atoms in this state, the maximum possible intensity of laser light will be detected by the photodiode. Note that the red arrows in Figure 6C depict the trajectory of transitions induced by optical pumping.

Another consequence of optical pumping to the dark state is that since all atoms occupy the same state (with the same angular momentum) their atomic magnetic moments are aligned and they experience coherent spin precession. This coherence means the gas in the vapour cell is highly polarised along the direction of the laser beam and as a result, it has a strong net magnetisation along this axis. Any small change in the external magnetic field will exert a torque on this net magnetisation, and hence precession of the bulk magnetisation in accordance with the Bloch equations (see below).

3.4. Maintaining spin polarisation with the SERF regime

A major challenge is that relaxation effects destroy coherence and therefore the net magnetisation. For an OPM to work, these effects must be mitigated. The dominant source of relaxation is spin-exchange collisions. As explained above, the direction of electron spin precession depends on which hyperfine state ($F = 1$ or $F = 2$) the atom is in, due to the opposite sign of their gyromagnetic ratios. In a collision between two ^{87}Rb atoms, the overall angular momentum is preserved (meaning that the sum of m_F for the two atoms remains the same after the collision). However, there may be a change to the hyperfine levels. If before the collision, two atoms were both in the $F = 2$ state, they were precessing coherently in the same direction. However, if one of the atoms moves to the $F = 1$ state as a result of the collision, they will now be precessing in opposite directions. This contributes to a loss of coherence, which is characterised by a spin-exchange relaxation rate

$$R_{se} = \frac{1}{T_{se}}, \quad (14)$$

where T_{se} is the time between spin-exchange collisions.

Counterintuitively, OPMs use this effect to their advantage, optimising the environment in the cell to *increase* spin-exchange collisions. This is known as the Spin Exchange Relaxation Free (SERF) regime. To achieve SERF, the OPMs must be operated in a low field environment and with sufficiently high atomic density in the vapour cell (typically $1.5 \times 10^{-14} \text{cm}^{-3}$). These conditions lead to a spin-exchange rate that is much higher than the precession frequency ($R_{se} \gg \gamma B$), meaning the atoms rapidly switch between hyperfine states, changing direction of precession. In addition, the angle swept by the precessing spin between collisions is small. Despite only sweeping through a small angle, due to the higher number of available $F = 2$ states (five m_F sublevels for $F = 2$ and three for $F = 1$) there is a coherent, net positive precession which occurs at a reduced precessional frequency given by

$$\omega_0 = \frac{\gamma B}{Q(P)}, \quad (15)$$

where $Q(P)$ is the nuclear slowing down factor, which is a function of the polarisation of the system, P . When all the atoms are in the ($F = 2, m_F = 2$) state, spin-exchange collisions have no effect since there are no higher available m_F states to allow a transfer of angular momentum to occur. However, once the spins have started to depolarise, they are distributed over the allowed m_F sublevels and rapid switching between hyperfine states occurs, decreasing the average precessional frequency. For atoms with $I = 3/2$ such as ^{87}Rb , the nuclear slowing down factor $Q(P)$ is

$$Q(P) = \frac{6 + 2P^2}{1 + P^2}. \quad (16)$$

By operating in the SERF regime, the coherence time and the atomic density of the magnetometer is increased, making it a viable magnetometer.

3.5. Signal equations

The combination of optical pumping and SERF induces a polarisation, \mathbf{P} , which, in the presence of an external magnetic field, \mathbf{B} , can be described by the Bloch equations [56] such that,

$$\frac{d\mathbf{P}}{dt} = \frac{1}{Q(P)} \left[\gamma \mathbf{P} \times \mathbf{B} - (\mathbf{P} - P_0 \hat{z}) \frac{1}{T} \right], \quad (17)$$

where P_0 is the equilibrium polarisation due to optical pumping when the external magnetic field is zero. T is a time constant that combines the optical pumping rate, R , and the relaxation time, T_2 so that $T = \left(R + \frac{1}{T_2} \right)^{-1}$. If we assume that the direction of the laser beam

is in z , Equation 17 can be solved in the steady state ($\frac{d\mathbf{P}}{dt} = 0$) and expanded into its vector components to give

$$\begin{aligned} P_x &= \frac{\frac{B_y}{\gamma T} + B_x B_z}{\left(\frac{1}{\gamma T}\right)^2 + B_x^2 + B_y^2 + B_z^2} P'_0 \\ P_y &= \frac{-\frac{B_x}{\gamma T} + B_y B_z}{\left(\frac{1}{\gamma T}\right)^2 + B_x^2 + B_y^2 + B_z^2} P'_0 \\ P_z &= \frac{\left(\frac{1}{\gamma T}\right)^2 + B_z^2}{\left(\frac{1}{\gamma T}\right)^2 + B_x^2 + B_y^2 + B_z^2} P'_0 \end{aligned} \quad (18)$$

where $P'_0 = P_0 RT$. In a vector magnetometer, we aim to measure the field perpendicular to the direction of the laser beam (say, B_x , since the laser beam is propagating in the z -direction). If we assume that $B_y = B_z = 0$, then the above equations simplify to

$$\begin{aligned} P_x &= 0 \\ P_y &= \frac{-\gamma T B_x}{1 + (\gamma T B_x)^2} P'_0 \\ P_z &= \frac{1}{1 + (\gamma T B_x)^2} P'_0. \end{aligned} \quad (19)$$

A plot of the solutions as a function of B_x is shown in Figure 6D. Thus, the component of polarisation along the direction of the laser beam, P_z , which we can measure via assessment of light through the cell, changes as a Lorentzian function of B_x , termed a zero-field resonance. Whilst in principle this offers a viable magnetometer, outputs are extremely sensitive to $1/f$ noise, and it is hard to differentiate between positive and negative fields due to the symmetric nature of the Lorentzian.

To combat this, an oscillating magnetic field is applied using onboard-sensor coils (a small square Helmholtz pair) in the direction of measurement, B_x . This modulates the amplitude of the polarisation with a frequency much higher than the relaxation rate of the vapour in the cell. Equation 17 must now be redefined to include the oscillating field so that

$$\frac{d\mathbf{P}}{dt} = \frac{1}{Q(P)} \left[\gamma \mathbf{P} \times [\mathbf{B} + b_x \sin \omega t \hat{x}] - (\mathbf{P} - P_0 \hat{z}) \frac{1}{T} \right], \quad (20)$$

where b_x is the amplitude of the modulation field and ω is its angular frequency. The equation then becomes time-varying, meaning the steady state solution is no longer valid and a new solution to the Bloch equation is required. Evaluating P_z in this case [57] gives

$$P_z = \frac{\gamma T B_x}{1 + (\gamma T B_x)^2} J_0\left(\frac{\gamma b_x}{Q(P)\omega}\right) J_1\left(\frac{\gamma b_x}{Q(P)\omega}\right) P_0' \sin \omega t, \quad (21)$$

where J_n are Bessel functions of the first kind [58,59]. Both J_1 and J_2 evaluate to a constant and can, along with P_0' , be absorbed into a constant. The voltage signal detected at the photodiode can therefore be given as

$$V_x \propto \frac{\gamma T B_x}{1 + (\gamma T B_x)^2} \sin \omega t. \quad (22)$$

Lock-in detection is then used at the photodiode leaving the final signal equation

$$V_x \propto \frac{\gamma T B_x}{1 + (\gamma T B_x)^2}. \quad (23)$$

Figure 6E shows V_x as a function of B_x . There is an area around zero field where the curve is approximately linear and allows for easy distinction between positive and negative signals. Fields within this range can be approximated using the Taylor expansion of Equation 23, thus (where $\gamma T B_x \ll 1$)

$$V_x \propto \gamma T B_x. \quad (24)$$

This linearity in the response is shown in Figure 6E and allows the change in magnetic field to be measured from a simple field per unit voltage conversion given by the slope (or gain). However, note the relatively small dynamic range; outside the range where the response is linear ($\sim \pm 1.5$ nT) the output becomes unreliable. It is also important to note that this solution relies on the assumption that B_y and B_z are zero. As we will see, deviation from this will lead to changes in the response.

The above focuses on how OPMs measure the magnetic field in a single direction (B_x) perpendicular to the direction of the laser beam. However, if orthogonal modulation fields in the x and y directions are applied simultaneously, the magnetic field can be measured along both axes simultaneously. As explained above, to extend this to three axes requires two orthogonal laser beams and two photodiodes. The first beam is oriented along the z-axis and can be used to measure fields in x and y, while the second is oriented along the x-axis and can be used to measure fields in y and z. This leads to four simultaneous measurements, two measurements of B_y that are averaged together and a single measurement of B_x and B_z .

3.6. OPM operation in reality

As previously mentioned, operation of OPMs requires a low field environment and there are several reasons for this. First, the SERF regime requires low field so that $R_{sc} \gg \gamma B$. The onboard coils in the OPM can null fields up to several tens of nanotesla; however, the field inside the MSR must still be lower than this if the sensor is to work. Second, as shown in Figure 6E, the sensor response is only linear within a range of approximately $\pm 1.5\text{nT}$; if background fields along the measurement direction become larger than this (either due to environmental changes, or movement of the OPM relative to a static field) then assumptions on sensor gain become invalid. Finally, to compound this problem, it is extremely unlikely that background fields will only exist in the measurement orientation and so the assumption that $B_y = B_z = 0$ is most often not the case. In this more complex case then the solution to the Bloch equations becomes

$$V_x \propto -J_0 \left(\frac{\gamma b_x}{Q(P)\omega} \right) J_1 \left(\frac{\gamma b_x}{Q(P)\omega} \right) \times \frac{\frac{1}{T} \gamma B_x + \gamma^2 J_0^2 \left(\frac{\gamma b_x}{Q(P)\omega} \right) B_y B_z}{\frac{1}{T^2} + \gamma^2 B_x^2 + J_0^2 \left(\frac{\gamma b_x}{Q(P)\omega} \right) \gamma^2 B_y^2 + J_0^2 \left(\frac{\gamma b_x}{Q(P)\omega} \right) \gamma^2 B_z^2}, \quad (25)$$

where V_x is the sensor output and B_x is the desired field [60]. The inclusion of B_y and B_z terms changes the shape of the response and therefore the sensor gain, as shown in Figure 7. This means that for a constant B_x , changes in B_y and B_z lead to errors in the measurement. This effect is known as cross-axis projection error or CAPE [43].

It follows that the magnetic field across the OPM cell must be kept as close to zero as possible to avoid gain errors. There are two options to achieve this. Firstly the OPMs can be operated in a ‘closed-loop’ mode, where the zero-field environment is maintained through a negative feedback loop [61] [62]. The currents applied to the onboard coils are updated based on the field measured, continuously returning the field in the cell to zero. From Equation 25, it is clear that sensitivity to all three axes is required for closed-loop operation to work, highlighting further the benefit of triaxial sensors. Alternatively, a combination of passive and active magnetic shielding can be used to reduce the magnetic field across the whole OPM array – if this is reduced to $< 1\text{nT}$ then the CAPE effect is negated [43] even in the absence of closed loop operation.

3.7. Enabling OPM-MEG

3.7.1. Passive shielding—Passive shielding refers to techniques involving enclosing experimental setups using specific materials to screen magnetic fields that would otherwise interfere with MEG data and/or render OPMs inoperable. We have already discussed the requirement of a MSR to attenuate the Earth’s magnetic field. However, the MSR needs to be able to screen both static fields (such as the Earth’s field) and time-varying fields (e.g. those from passing vehicles and mains electricity); such environmental fields are often larger than those generated by the body. The MSR therefore involves careful design and choice of materials to account for the different shielding requirements.

For low frequency (DC) fields a mechanism called flux shunting is employed [63]. Flux shunting works based on the behaviour of a magnetic field when it reaches an interface between materials (in this case air and the shielded room). There are two conditions that must be met to satisfy both Ampere's law and Gauss' law in this case. Firstly, to satisfy Ampere's law, the tangential component of the magnetic field, \mathbf{H} , must be continuous across the boundary. Secondly, Gauss' law states that the normal component of the magnetic flux density, \mathbf{B} , must also be continuous across the boundary. We also know that

$$\mathbf{B} = \mu_0 \mu_r \mathbf{H}, \quad (26)$$

which simplifies to $\mathbf{B} = \mu_0 \mathbf{H}$ in air since $\mu_r = 1$. If the walls of the MSR are made from a material with high magnetic permeability (such as MuMetal, a nickeliron alloy for which μ_r is typically between 80,000 and 100,000) then to satisfy both conditions, the direction of the external magnetic field must abruptly change at the interface. On the air side of the interface, the field becomes almost perpendicular to the surface of the MSR as it enters the walls. However, on the material side, the field is almost tangential to the surface. The field is essentially diverted into the wall of shield, once inside the shielding material it is 'shunted' in a direction almost parallel to the surface of the material and then it is 'released' back into the air.

For time-varying fields, eddy current cancellation becomes the dominant shielding mechanism. Time-varying (or AC) fields induce an electric field, \mathbf{E} , within a material according to Faraday's law

$$\nabla \times \mathbf{E} = - \left(\frac{\partial \mathbf{B}}{\partial t} \right). \quad (27)$$

For materials with an electrical conductivity, σ , the induced electric field causes an induced current density in the material. The induced current produces a resulting magnetic flux which opposes the change in imposed magnetic flux from the time-varying field. This results in the imposed magnetic flux being diverted away from the material interface. For time-varying fields with an angular frequency $\omega = 2\pi f$ and permeability μ , the exponential decay of the induced current density into the material has a characteristic decay length

$$\delta = \sqrt{\frac{2}{\omega \mu_0 \mu_r \sigma}}, \quad (28)$$

where δ is referred to as the 'skin depth' of the material.

Logically, the ideal case would be to have a skin depth much smaller than the thickness of the shield, t . However, for copper and aluminium respectively, the skin depths are $\delta = 8.5 \text{ mm}$ and $\delta = 11.8 \text{ mm}$, making it impractical to meet this condition. Significant shielding

can still be achieved with $\delta \gg \Delta$ if larger dimensions are used for the shield. When the induced current circulates around the large dimensions of the MSR wall it can produce an induced flux density which is comparable in magnitude to the imposed flux density of the time-varying field.

These two effects point to an optimum shielding solution using an MSR made from multiple layers, including a high permeability layer for shielding DC fields and a copper or aluminium layer for eddy current cancellation. Shielding performance increases with the number high permeability layers present, so an MSR for MEG is typically made with at least two layers of MuMetal.

The total effect of the passive shielding is known as the shielding factor and is simply given as

$$SF = \frac{|\mathbf{B}_0|}{|\mathbf{B}_s|}, \quad (29)$$

where $|\mathbf{B}_0|$ is the magnitude of the magnetic field at a single point in the absence of shielding and $|\mathbf{B}_s|$ is the magnitude of the same magnetic field at the same point once enclosed in the shielded environment. Most MSRs can reduce the Earth's field to approximately 10–70nT using the above techniques, but this can be reduced to around 5nT using a process called degaussing, where a sinusoidal linearly decaying AC current is applied to the MSR to drive the MuMetal around its hysteresis curve and remove the remnant magnetisation in the MSR walls. However, even a remnant field as low as 5nT is too large to enable movement in OPM-MEG, due to the effects inherent in Equation 25, and the fact that movement induced fields can obscure brain activity. Active shielding is therefore required in addition to the MSR.

3.7.2. Active shielding—Active shielding refers to the generation of an equal and opposite compensation magnetic field to further null the remnant field inside the MSR. Active shielding requires knowledge of the strength and spatial variation of the remnant field, which is often achieved by modelling the field as a series of spherical harmonics [42,64,65].

Briefly, we assume that the MSR is a current-free space and the remnant field \mathbf{B} can therefore be modelled as a magnetic scalar potential, Φ , i.e. that

$$\mathbf{B} = -\nabla\Phi. \quad (30)$$

To ensure that the magnetic field obeys Maxwell's equations in a current-free region

$$\nabla \cdot \mathbf{B} = 0, \quad (31)$$

and

$$\nabla \times \mathbf{B} = 0, \quad (32)$$

we must set

$$\nabla^2 \Phi = 0. \quad (33)$$

From Equation 33, the scalar potential, Φ , satisfies Laplace's equation and therefore its solutions can be represented as a series of real spherical harmonics. As sources of remnant field are distal to the sensor array (and will therefore vary slowly across space) we can reasonably approximate the magnetic field variation over the central region of the MSR using only the first and second order terms in the scalar potential (note that zeroth order terms are omitted as these describe a magnetic monopole). The three first order terms describe the three spatially uniform magnetic field components (i.e. describing a field has the same strength and direction at each position) which in cartesian coordinates are expressed as

$$\begin{aligned} \mathbf{B}_x &= a_1 \hat{x} \\ \mathbf{B}_y &= a_2 \hat{y} \\ \mathbf{B}_z &= a_3 \hat{z}, \end{aligned} \quad (34)$$

and the second order terms represent the five magnetic field gradient components (i.e. magnetic fields which vary linearly with their spatial position)

$$\begin{aligned} \mathbf{G}_{xy} &= a_4(y\hat{x} + x\hat{y}) \\ \mathbf{G}_{xz} &= a_5(z\hat{x} + x\hat{z}) \\ \mathbf{G}_{yz} &= a_6(z\hat{y} + y\hat{z}) \\ \mathbf{G}_{zz} &= a_7(-x\hat{x} - y\hat{y} + 2z\hat{z}), \mathbf{G}_{xx} = a_8(x\hat{x} - y\hat{y}) \end{aligned} \quad (35)$$

where α_n is the magnitude of the n^{th} component and \hat{x} , \hat{y} and \hat{z} are the Cartesian unit vectors. Higher order components can also be modelled [66], however most active shielding systems for MEG that have been developed to date only use the first 8 components.

Once modelled, to compensate a series of electromagnetic coils capable of generating each term in the spherical harmonic model is required. Usually, this is a series of 8 coils, three to produce uniform fields and five to produce field gradients. From knowledge of the strength of each component produced by each coil one can calculate a set of nulling coil currents to cancel the remnant field. Several techniques to obtain the coil currents and different coil set ups have emerged. For example, bi-planar coil designs have a set of 8 dedicated coils formed from wire paths placed on two large planes placed either side of the participant (one for each component of the field) [42]. The participant sits in the central region between

the planes and a set of reference sensors placed near the participants head can be used to coarsely estimate each of the 8 field components B_x , B_y and B_z and the five gradient terms (calculated by subtracting the B_x field of two different reference sensors, for example). The sensors are operated in a ‘field-zeroing’ mode, usually used to prepare the sensor for operation in which the static field up to 50nT is measured, so that the necessary currents can be applied to the on-board coils for internal nulling [42]. This field measurement is fed back to a PID (proportional integral derivative) controller, which drives the currents applied to the bi-planar coils to null the central region where the head sits. These nulling currents can be fixed for the duration of an experiment or can be dynamically updated throughout a recording to account for field drift inside the MSR [67,68]. Further advancement in this technique has seen more precise control of the background field using head-mounted OPMs to sample the field at many positions inside the MSR through combination of optical tracking cameras and a series of head rotations and translations which allow a participant to naturally ‘map’ the magnetic field that will be experienced by their likely movements during a scan [45].

In addition to bi-planar coils, other systems have employed Helmholtz or Helmholtz-like systems [69], and multi-coil systems where multiple simple coils are placed onto the walls of a MSR and coil currents chosen that shape the resulting field from all coils into spherical harmonic forms [65,66]. Multi-coil systems are attractive as they are simpler to manufacture and permit flexible coil design and placement and can be used to generate harmonics in volumes away from the centre of the windings. Other advancements include designs for coils with windings which occupy five of the six faces of the MSR [70], open-source coil design packages which allow coil windings to be distributed onto arbitrary surfaces [71], techniques to mitigate the effect of the MSR on the fields produced by coil systems (a change in field per unit current and decrease in the homogeneity of produced field from the designed performance [72]) and methods to utilise coil systems as a means of array calibration [65].

4. Future directions

Progress in the field of OPM-MEG has been rapid, from single sensor arrays with large and heavy sensors, to high-density lightweight wearable arrays that, combined with advancements in shielding, allow for fundamentally new opportunities to probe the human brain. The advantages of OPM-MEG can be summarised by four points:

1. **Better data:** Sensor proximity offers a higher signal strength and improved spatial resolution whilst the flexibility of OPM design enables simultaneous measurement of multiple field components, decreasing the impact of interference and consequently increasing SNR.
2. **Flexibility of sensor placement:** Because sensors are small and lightweight, they can be mounted on the scalp surface; meaning a system can adapt to any head shape or size, giving the best possible coverage in any participant from newborn baby to elderly adult. In addition, the array can be reconfigured to scan other areas of the body, e.g. heart, spine, muscles, or even the human foetus.

3. **Motion robustness:** Sensors move with the head, meaning that, assuming background fields are controlled appropriately, tasks can be carried out with a far greater range of head movement than was ever possible in conventional neuroimaging. This has significant advantages for experimental design, allowing naturalistic stimulation. It also allows new cohorts (e.g. children) who find conventional imaging environments challenging to be scanned.
4. **Simplicity:** With no reliance on low temperature sensors, OPM-MEG is simpler than conventional MEG, negating the use of liquid helium and liquification plants. Consequently, it has the potential to be lower cost, and more environmentally sustainable.

These advantages combined are likely to make OPM-MEG the method of choice for high fidelity mapping of human brain electrophysiology.

Like most medical imaging technologies, OPM-MEG is rooted in fundamental physics and as we have seen, a combination of quantum mechanics (for sensor operation) and advanced electromagnetism (for shielding) underpin the technology. The rapid rate of development shows no signs of stopping and current work indicates the next few years will see further significant improvements: advances in sensor design will likely see noise floors drop even further, helping to better translate the proximity advantages into SNR gains. Closed-loop mode, and better coil design will allow a greater range of motion (e.g. ambulatory motion) without saturating the sensor output. Higher density arrays will undoubtedly enhance both sensitivity and spatial resolution by better sampling the (very focal) fields that exist at the scalp surface (at the time of writing even the most advanced OPM systems have < 200 channels whereas conventional systems have > 300). Finally, enhancements in electronics for system control will likely see improvements in robustness, as well as further new opportunities, for example real time neurofeedback, and integration with neurostimulation techniques including e.g. transcranial magnetic stimulation. Perhaps most significantly, the coming years will likely see OPM-MEG gain medical device approval, meaning that OPM-MEG can begin to realise its true value as a clinical device, with obvious initial applications in the management of epilepsy patients.

Human brain health is perhaps the biggest challenge facing the twenty-first century healthcare. History shows that fundamental physics is at the heart of modern healthcare, with technologies like MRI changing the lives of millions. OPM-MEG is perhaps the latest example of this. It is currently a nascent technology, but even at this early stage the rapid development and commercialisation has seen it become a disruptive tool in the functional neuroimaging field – at least for research. As the field moves forward, it's tempting to speculate that OPM-MEG could become a ubiquitous tool for clinical assessment.

Biographies

Holly Schofield is a Ph.D. student at the University of Nottingham, where she also obtained her Master's degree in Physics. Her research focuses on advancing the use of OPMS for magnetoencephalography. She also works as a scientific researcher for Cerca Magnetics Limited on neuroimaging system development.

Elena Boto has been the lead author on many of the papers which have led to the neuroimaging community considering wearable technology as a viable alternative to the current state of the art. Elena was originally trained in physics at the Universidad Complutense in Madrid, and has a Ph.D. in Physics from the University of Nottingham. She is co-founder and chief technology officer of Cerca Magnetics Limited, working on bringing OPM-MEG technology to research groups around the world.

Vishal Shah is Chief Scientist at QuSpin. He spent much of his academic career focusing on the development of atomic magnetometers, obtaining his Ph.D in Atomic Physics from the University of Colorado Boulder before working on developing portable scalar and ultra-sensitive spin-exchange relaxation free magnetometers as a Postdoc at Princeton University. He founded QuSpin in 2012 and has since commercialised the first OPM sensors.

Ryan M. Hill has been working with OPM-MEG since 2017, developing novel hardware and software techniques. He has been lead author on papers detailing the first paediatric application of OPM-MEG, and the first demonstration of an OPM-MEG system with whole head coverage. Ryan achieved his Master's degree in Physics and Ph.D from the University of Nottingham.

James Osborne is a skilled engineer working at QuSpin Inc. on the research and development of optically pumped magnetometers. Specifically, his work has been centred on generating the software and firmware which controls the OPMs. He obtained his Bachelor of Science in Engineering Physics from the University of Colorado Boulder.

Molly Rea Following undergraduate training in physics, Molly completed her Ph.D at the University of Nottingham in 2022. Her work focused on using active shielding to enable and improve data quality in paradigms with high levels of subject movement. She now works as a senior scientist at Cerca Magnetics Limited delivering OPM-MEG systems to research teams around the world.

Cody Doyle is an accomplished engineer with degrees in Physics from both the Colorado School of Mines and the University of Alabama in Huntsville. Currently, he is a key member of the team at QuSpin, where he focuses on developing ultrahigh sensitivity magnetometers for bioimaging applications. His research interests lie at the intersection of magnetometry and neuroscience, with a particular emphasis on magnetoencephalography and brain-computer interfaces.

Niall Holmes has been developing hardware and techniques to enable wearable neuroimaging since 2016 and is the lead author on papers describing electromagnetic coil systems which have been commercialised and sold internationally. He was trained in Medical Physics at the University of Nottingham, where he also obtained his Ph.D.

Richard Bowtell has more than 35 years' experience of developing novel biomedical imaging systems, with a particular interest in electromagnetic coil design for both magnetic resonance imaging, and more recently wearable MEG. Richard is a Fellow of the Institute of Physics and of the International Society of Magnetic Resonance in Medicine and is Past

President of the European Society of Magnetic Resonance in Medicine and Biology, as well as director of the Sir Peter Mansfield Imaging Centre at the University of Nottingham.

David Woolger is chief executive officer of Cerca Magnetics Limited as well as Managing Director of Magnetic Shields Limited. He worked at Deloitte as Management Consultant for 9 years. He is a CIMA qualified accountant, and his standing in the UK quantum technologies community is well recognised, for example by his membership of the UK Quantum ATEP Board.

Matthew J. Brookes is professor of Physics at the University of Nottingham, working on the development and application of human neuroimaging. Specifically, he works in the fields of hardware development, mathematical modelling and measurement of functional connectivity. His most recent work has been on the applications of quantum technologies to electrophysiological brain imaging.

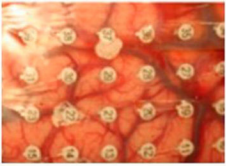



References

- [1]. Mansfield P, Pykett IL. Biological and medical imaging by NMR. *J Mag Reson* (1969). 1978;29(2):355–373.
- [2]. Ambrose J, Hounsfield G Computerized transverse axial tomography. *Br J Radiol*. 1973;46(542):148–9. [PubMed: 4686818]
- [3]. Reif PS, Strzelczyk A, Rosenow F. The history of invasive EEG evaluation in epilepsy patients. *Seizure*. 2016;41:191–195. [PubMed: 27131772]
- [4]. Ogawa S, et al. Brain magnetic resonance imaging with contrast dependent on blood oxygenation. *Proc Natl Acad Sci U S A*. 1990;87(24):9868–72. [PubMed: 2124706]
- [5]. Phelps ME, et al. Application of annihilation coincidence detection to transaxial reconstruction tomography. *J Nucl Med*. 1975;16(3):210–224. [PubMed: 1113170]
- [6]. Jöbsis FF. Noninvasive, infrared monitoring of cerebral and myocardial oxygen sufficiency and circulatory parameters. *Science*. 1977;198(4323):1264–7. [PubMed: 929199]
- [7]. Berger H Über das elektrenkephalogramm des menschen. *Archiv für Psychiatrie und Nervenkrankheiten*. 1929;87(1):527–570.
- [8]. Cohen D Magnetoencephalography: detection of the brain’s electrical activity with a superconducting magnetometer. *Science*. 1972;175(4022):664–666. [PubMed: 5009769]
- [9]. Sadaghiani S, et al. , Connectomics of human electrophysiology. *NeuroImage*. 2022;247:118788. [PubMed: 34906715]
- [10]. Xia H, et al. Magnetoencephalography with an atomic magnetometer. *Appl Phys Lett*. 2006;89(21):211104.
- [11]. Johnson CN, Schwindt PD, Weisend M. Multi-sensor magnetoencephalography with atomic magnetometers. *Phys Med Biol*. 2013;58(17):6065–77. [PubMed: 23939051]
- [12]. Borna A, et al. A 20-channel magnetoencephalography system based on optically pumped magnetometers. *Phys Med Biol*. 2017;62(23):8909–8923. [PubMed: 29035875]
- [13]. Shah VK, Wakai RT. A compact, high performance atomic magnetometer for biomedical applications. *Phys Med Biol*. 2013;58(22):8153–8161. [PubMed: 24200837]
- [14]. Borna A, et al. Non-Invasive functional-brain-imaging with an OPM-based magnetoencephalography system. *PLOS ONE*. 2020;15(1):e0227684. [PubMed: 31978102]
- [15]. An K. m., et al. Detection of the 40-Hz auditory steady-state response with optically pumped magnetometers. *Sci. Rep*. 2022;12(1):17993. [PubMed: 36289267]
- [16]. Boto E, et al. A new generation of magnetoencephalography: room temperature measurements using optically pumped magnetometers. *Neuroimage*. 2017;149:404–414. [PubMed: 28131890]
- [17]. Sander TH, et al. Magnetoencephalography with a chip-scale atomic magnetometer. *Biomed Opt Expr*. 2012;3(5):981–90.

- [18]. Labyt E, et al. Magnetoencephalography With optically pumped (4)He magnetometers at ambient temperature. *IEEE Trans Med Imag.* 2019;38(1):90–98.
- [19]. Rhodes N, et al. Measurement of Frontal Midline Theta Oscillations Using OPM-MEG. 2023.
- [20]. Lin CH, et al. Using optically pumped magnetometers to measure magnetoencephalographic signals in the human cerebellum. *J Physiol.* 2019;597(16):4309–4324. [PubMed: 31240719]
- [21]. Boto E, et al. Moving magnetoencephalography towards real-world applications with a wearable system. *Nature.* 2018;555(7698):657–661. [PubMed: 29562238]
- [22]. Tierney TM, et al. Cognitive neuroscience using wearable magnetometer arrays: Non-invasive assessment of language function. *NeuroImage.* 2018;181:513–520. [PubMed: 30016678]
- [23]. Hill RM, et al. Multi-channel whole-head OPM-MEG: helmet design and a comparison with a conventional system. *NeuroImage.* 2020;219:116995. [PubMed: 32480036]
- [24]. Iivanainen J, Zetter R, Parkkonen L. Potential of on-scalp MEG: robust detection of human visual gamma-band responses. *Hum Brain Map.* 2020;41(1):150–161.
- [25]. de Lange P, et al. Measuring the cortical tracking of speech with optically-pumped magnetometers. *NeuroImage.* 2021;233:117969. [PubMed: 33744453]
- [26]. Boto E, et al. Measuring functional connectivity with wearable MEG. *NeuroImage.* 2021;230:117815. [PubMed: 33524584]
- [27]. Rea M, et al. A 90-channel triaxial magnetoencephalography system using optically pumped magnetometers. *Ann NY Acad Sci.* 2022;1517(1):107–124. [PubMed: 36065147]
- [28]. An N, et al. Imaging somatosensory cortex responses measured by OPM-MEG: variational free energy-based spatial smoothing estimation approach. *iScience.* 2022;25 (2): 103752. [PubMed: 35118364]
- [29]. Boto E, et al. On the potential of a New generation of magnetometers for MEG: A beamformer simulation study. *PLOS ONE.* 2016;11(8):e0157655. [PubMed: 27564416]
- [30]. Iivanainen J, Stenroos M, Parkkonen L. Measuring MEG closer to the brain: performance of on-scalp sensor arrays. *NeuroImage.* 2017;147:542–553. [PubMed: 28007515]
- [31]. Barry DN, et al. Imaging the human hippocampus with optically-pumped magnetoencephalography. *NeuroImage.* 2019;203:116192. [PubMed: 31521823]
- [32]. Tierney TM, et al. Mouth magnetoencephalography: A unique perspective on the human hippocampus. *NeuroImage.* 2021;225:117443. [PubMed: 33059052]
- [33]. Lin C-H, et al. Using optically pumped magnetometers to measure magnetoencephalographic signals in the human cerebellum. *J Physiol.* 2019;597(16):4309–4324. [PubMed: 31240719]
- [34]. Boto E, et al. Wearable neuroimaging: combining and contrasting magnetoencephalography and electroencephalography. *Neuroimage.* 2019;201:116099. [PubMed: 31419612]
- [35]. Nugent AC, et al. On-scalp magnetocorticography with optically pumped magnetometers: simulated performance in resolving simultaneous sources. *Neuroim Rep.* 2022;2(2):100093.
- [36]. Rampp S, et al. Magnetoencephalography for epileptic focus localization in a series of 1000 cases. *Brain.* 2019;142(10):3059–3071. [PubMed: 31373622]
- [37]. Shah V, Osborne J, Doyle C. Zero field parametric resonance magnetometer with triaxial sensitivity. United States: QuSpin, Inc.; 2020.
- [38]. Boto E, et al. Triaxial detection of the neuromagnetic field using optically-pumped magnetometry: feasibility and application in children. *NeuroImage.* 2022;252: 119027. [PubMed: 35217205]
- [39]. Sarvas J Basic mathematical and electromagnetic concepts of the biomagnetic inverse problems. *Phys Med Biol;* 1987(32):11–22. [PubMed: 3823129]
- [40]. Brookes MJ, et al. Theoretical advantages of a triaxial optically pumped magnetometer magnetoencephalography system. *NeuroImage.* 2021;236:118025. [PubMed: 33838266]
- [41]. Rier L, et al. Test-Retest Reliability of the Human Connectome: An OPM-MEG study. *bioRxiv,* 2022: p. 2022. 12.21.521184.
- [42]. Holmes N, et al. A bi-planar coil system for nulling background magnetic fields in scalp mounted magnetoencephalography. *NeuroImage.* 2018;181:760–774. [PubMed: 30031934]

- [43]. Borna A, et al. Cross-Axis projection error in optically pumped magnetometers and its implication for magnetoencephalography systems. *NeuroImage*. 2022;247: 118818. [PubMed: 34915157]
- [44]. Roberts G, et al. Towards OPM-MEG in a virtual reality environment. *NeuroImage*. 2019;199:408–417. [PubMed: 31173906]
- [45]. Rea M, et al. Precision magnetic field modelling and control for wearable magnetoencephalography. *NeuroImage*. 2021;241:118401. [PubMed: 34273527]
- [46]. Seymour RA, et al. Using OPMs to measure neural activity in standing, mobile participants. *bioRxiv*, 2021: p. 2021.05.26.445793.
- [47]. Holmes N, et al. Naturalistic hyperscanning with wearable magnetoencephalography. *bioRxiv*, 2021: p. 2021.09.07. 459124.
- [48]. Hill RM, et al. A tool for functional brain imaging with lifespan compliance. *Nat Commun*. 2019;10:4785. [PubMed: 31690797]
- [49]. Feys O, et al. On-Scalp optically pumped magnetometers versus cryogenic magnetoencephalography for diagnostic evaluation of epilepsy in school-aged children. *Radiology*. 2022;304(2):429–434. [PubMed: 35503013]
- [50]. Hillebrand A, et al. Improved non-invasive detection of ictal and interictal epileptiform activity using Optically Pumped Magnetometers. *medRxiv*, 2022: p. 2022.11.03. 22281836.
- [51]. Feys O, et al. Recording of ictal epileptic activity using on-scalp magnetoencephalography. *Ann Neurol*. 2023;93(2):419–421. [PubMed: 36480016]
- [52]. Alem O, et al. Fetal magnetocardiography measurements with an array of microfabricated optically pumped magnetometers. *Phys Med Biol*. 2015;60(12):4797–4811. [PubMed: 26041047]
- [53]. Mardell LC, et al. Concurrent spinal and brain imaging with optically pumped magnetometers. *bioRxiv*, 2022: p. 2022.05.12.491623.
- [54]. Benumof R Optical pumping theory and experiments. *American Journal of Physics*. 1965;33(2):151–160.
- [55]. Zeeman P VII. Doublets and triplets in the spectrum produced by external magnetic forces. *Lond Edinburgh Dublin Philos Mag J Sci*. 1897;44(266):55–60.
- [56]. Bloch F Nuclear induction. *Phys Rev* 1946;70(7–8): 460–474.
- [57]. Cohen-Tannoudji C, et al. Diverses résonances de croisement de niveaux sur des atomes pompés optiquement en champ nul. I. Théorie *Rev Phys Appl (Paris)* 1970;5(1):95–101.
- [58]. Shah V, Romalis MV. Spin-exchange relaxation-free magnetometry using elliptically polarized light. *Phys Rev A*. 2009;80(1):013416.
- [59]. Tierney TM, et al. Optically pumped magnetometers: from quantum origins to multi-channel magnetoencephalography. *NeuroImage*. 2019;199:598–608. [PubMed: 31141737]
- [60]. Zhang S, et al. Triaxial precise magnetic field compensation of a zero-field optically pumped magnetometer based on a single-beam configuration. *Opt Expr*. 2022;30(14):24579–24588.
- [61]. Lee HJ, et al. Flat-response spin-exchange relaxation free atomic magnetometer under negative feedback. *Opt Expr*. 2014;22(17):19887–19894.
- [62]. Nardelli NV, et al. A conformal array of microfabricated optically-pumped first-order gradiometers for magnetoencephalography. *EPJ Quantum Technol*. 2020;7(1):11.
- [63]. Hoberg JF. Principles of quasistatic magnetic shielding with cylindrical and spherical shields. *IEEE Trans Electromag Compatib*. 1995;37(4):574–579.
- [64]. Mellor S, et al. Magnetic field mapping and correction for moving OP-MEG. *IEEE Trans Biomed Eng*. 2022;69(2):528–536. [PubMed: 34324421]
- [65]. Iivanainen J, et al. Calibration and localization of optically pumped magnetometers using electromagnetic coils. *Sensors*. 2022;22(8):3059. [PubMed: 35459044]
- [66]. Holmes N, et al. A lightweight magnetically shielded room with active shielding. *Sci Rep*. 2022;12(1):13561. [PubMed: 35945239]
- [67]. Holmes N, et al. Balanced, bi-planar magnetic field and field gradient coils for field compensation in wearable magnetoencephalography. *Sci Rep*. 2019;9(1):14196. [PubMed: 31578383]

- [68]. Hill RM, et al. Using OPM-MEG in contrasting magnetic environments. *Neuroimage*. 2022;253:119084. [PubMed: 35278706]
- [69]. Iivanainen J, et al. On-scalp MEG system utilizing an actively shielded array of optically-pumped magnetometers. *NeuroImage*. 2019;194:244–258. [PubMed: 30885786]
- [70]. Kutschka H, et al. Magnetic field compensation coil design for magnetoencephalography. *Sci Rep*. 2021;11(1): 22650. [PubMed: 34811388]
- [71]. Zetter R, et al. Magnetic field modeling with surface currents. part II. implementation and usage of bfieldtools. *J Appl Phys*. 2020;128(6):063905.
- [72]. Packer M, et al. Optimal inverse design of magnetic field profiles in a magnetically shielded cylinder. *Phys Rev Appl*. 2020;14(5):054004.

| Modality | iEEG | EEG | fMRI | fNIRS |
|----------------------------|-----------------------------------------------------------------------------------|------------------------------------------------------------------------------------|-------------------------------------------------------------------------------------|-------------------------------------------------------------------------------------|
| |  |  |  |  |
| Spatial Resolution | <1mm | ~50-90mm | ~1-2mm | ~10mm |
| Temporal Resolution | ~1ms | ~1ms | ~1-4s | ~10ms |
| Invasive | Requires surgery | Non-invasive | Non-invasive | Non-invasive |
| Wearability | Wearable but no free movement | Wearable | Not wearable | Wearable |



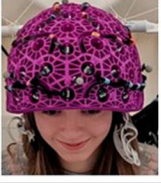
| Modality | PET | MEG | OPM-MEG |
|----------------------------|-----------------------------------------------------------------------------------|------------------------------------------------------------------------------------|-------------------------------------------------------------------------------------|
| |  |  |  |
| Spatial Resolution | 4-5mm | ~2-3mm | <2mm |
| Temporal Resolution | 5-10s | ~1ms | ~1ms |
| Invasive | Non-invasive but ionising | Non-invasive | Non-invasive |
| Wearability | Not wearable | Not wearable | Wearable inside shielded room |

Figure 1. Functional neuroimaging: A summary of commonly used methods to interrogate brain function. Image credits: iEEG (Adapted from Sadaghiani et al. [9]), EEG (Dr. Elena Boto - University of Nottingham), fMRI (University of Nottingham), fNIRS (Dr. Sam Lucas - University of Birmingham), PET (Jens Maus), MEG (Adapted from Boto et al. [20]), OPM-MEG (University of Nottingham).

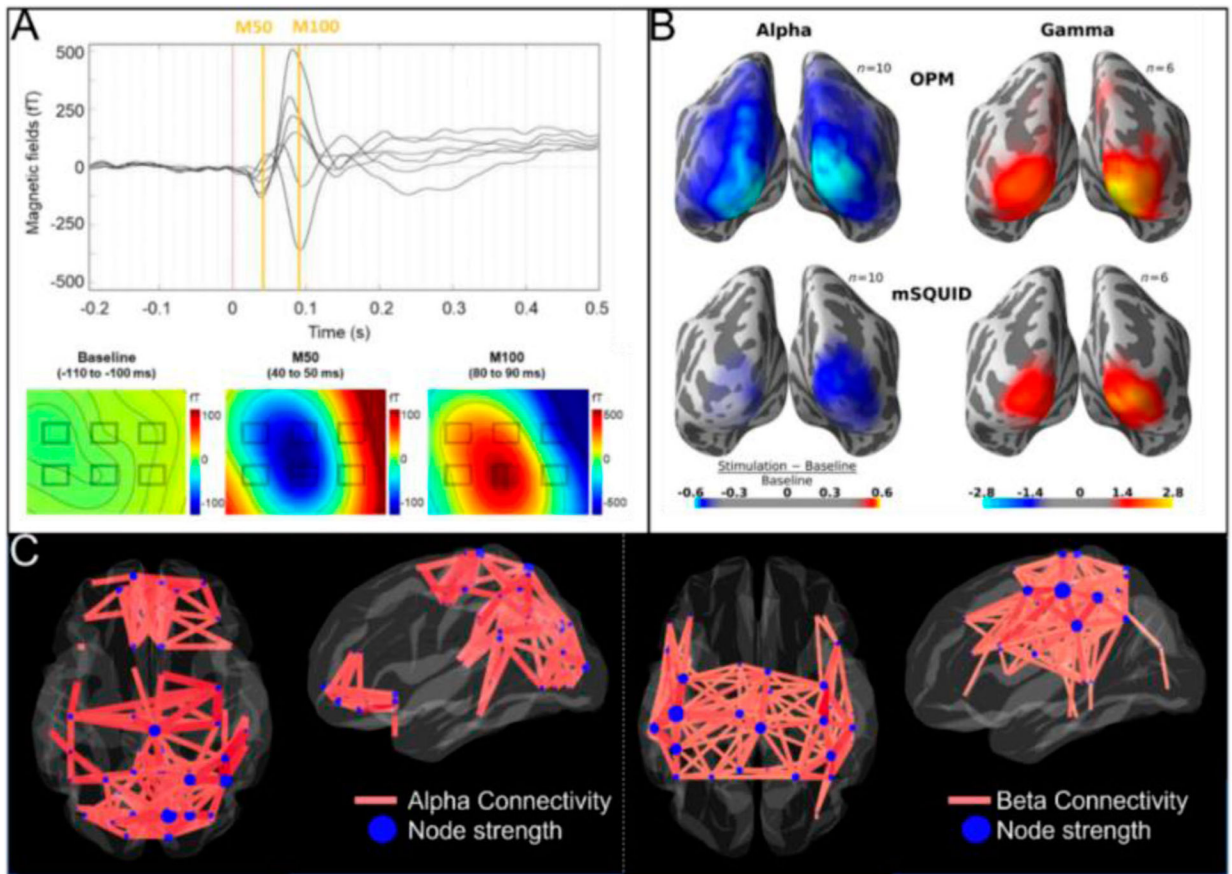


Figure 2. Example measurements using OPM-MEG. A) The auditory evoked response measured using 6 OPMs placed over the temporal lobe. The upper plot shows the temporal morphology. The lower plots show spatial topography at three timepoints. (Adapted from An et al. [15]) B) Source localised responses to visual stimulation using a moving circular grating. Left: alpha band power decrease; right: a gamma band increase. OPM measurements (top) are compared to measurements from an array of SQUID magnetometers (bottom). (Adapted from Iivanainen et al. [24]) C) Resting state connectivity measurements. The red lines show the strongest 300 connections between regions delineated using a brain parcellation. The blue dots show connectivity strength at each region. Left: networks in the alpha band; right: networks in the beta band. (Adapted from Boto et al. [26])

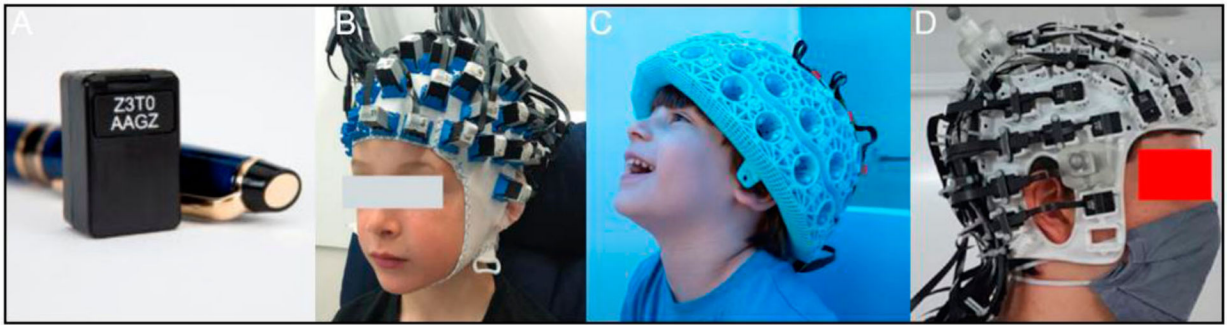


Figure 3.

A) A Gen-3 triaxial OPM sensor from QuSpin Inc. (Photo taken from <https://quspinc.com/products-qzfm/>). B) OPMs mounted into an EEG like cap (Adapted from Feys et al. [49]). C) A rigid helmet designed to fit most 4-year-olds (Cerca Magnetics www.cercamagnetics.com). D) A 3D printed bespoke helmet designed to perfectly fit a single individual (Chalk Studios, <http://www.chalkstudios.co.uk/>).

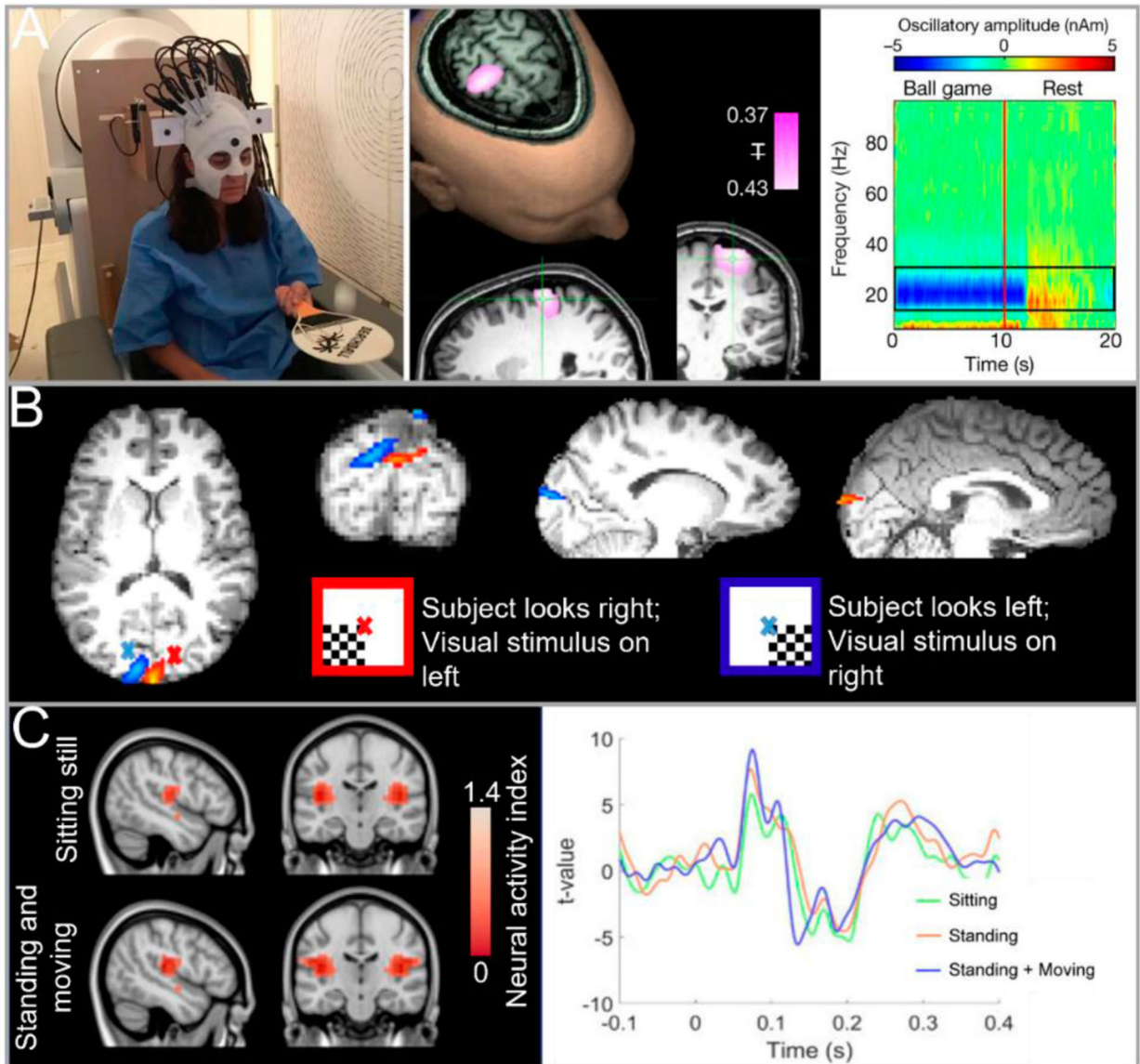


Figure 4.

Measuring brain activity during movement: A) Motor cortex activity measured as a subject bounced a ball on a bat (Left hand image). Beta band modulation was localised to the left sensorimotor cortex (Centre panel) and a time frequency analysis (right hand panel) shows movement related beta decrease during the game. (Adapted from Boto et al. [21]) B) A subject rotated their head to view a visual stimulus from two angles. The activity follows the retinotopic organisation of the visual cortex (blue overlay shows activity with the stimulus on the right; red overlay shows activity with the stimulus on the left) (Adapted from Holmes et al. [42]). C) Auditory evoked fields measured and localised to auditory cortex. Data were recorded with a subject seated, standing, and moving. Despite movement of up to 20” “ cm, both the localisation (left) and evoked response morphology (right) were consistent. (Adapted from Seymour et al. [46]).

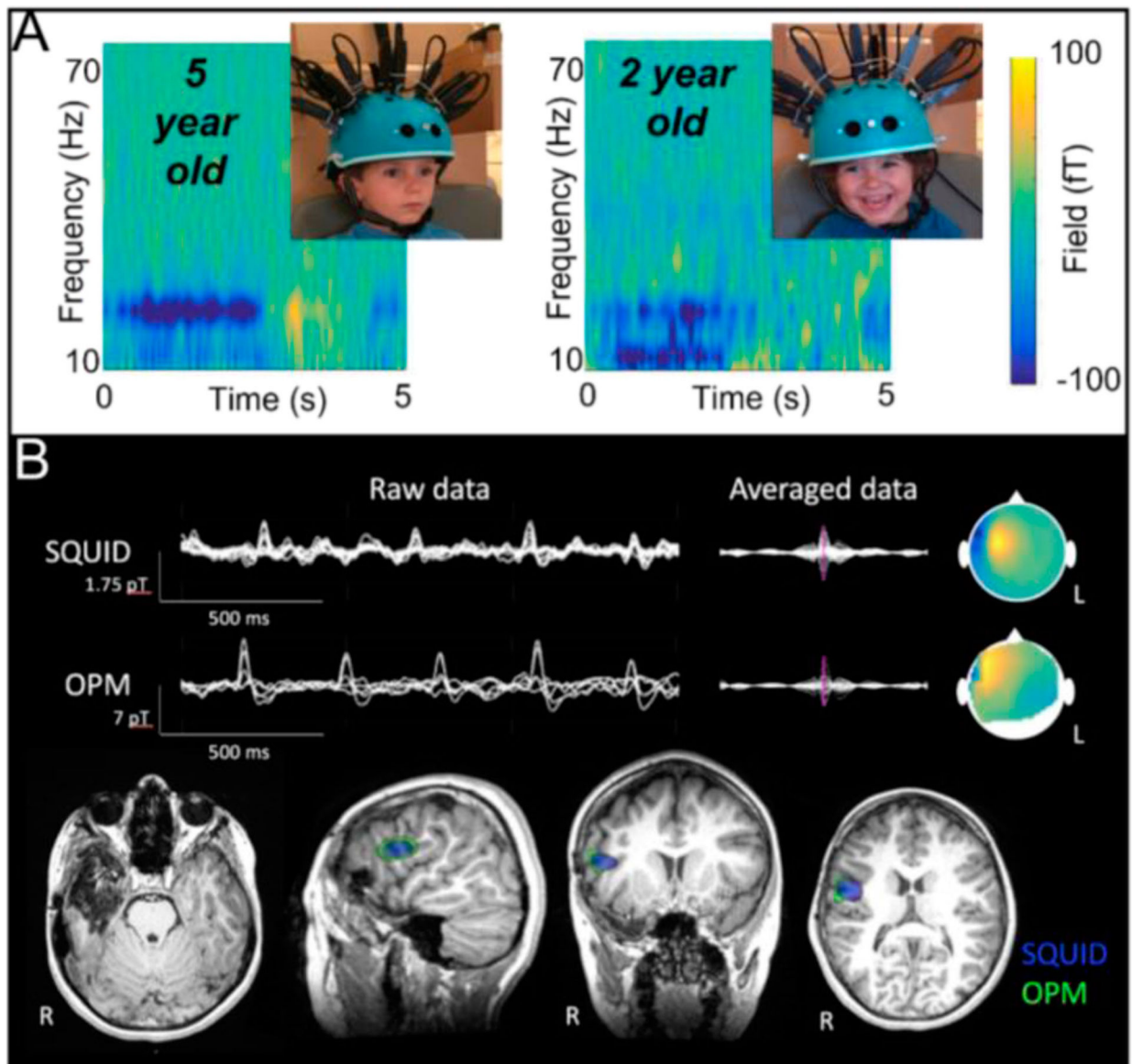
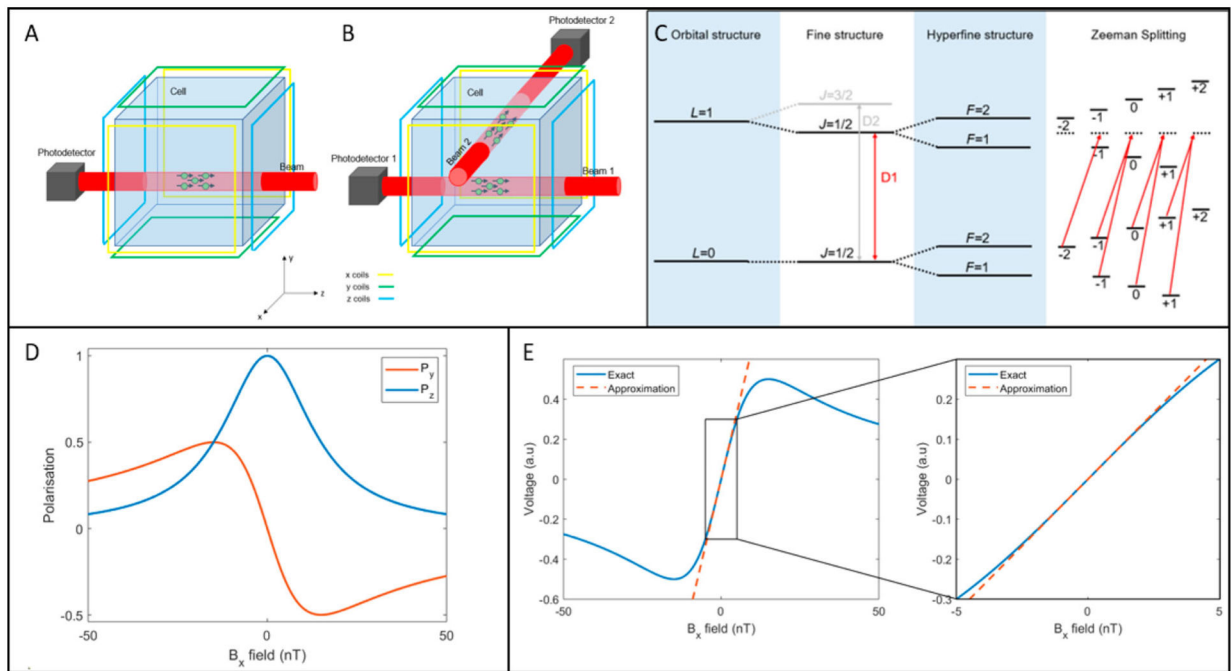


Figure 5. OPM-MEG measurements in children. A) A maternal touch paradigm in a 2 – and 5-year-old. The time-frequency spectrogram shows the expected drop in oscillatory amplitude during stimulation in the beta frequency band. (Adapted from Hill et al. [48]). B) epileptiform activity measured in children. The upper panel shows timecourses (unaveraged and averaged) from both SQUIDs and OPM's, showing clearly epileptic spikes; the field topographies are also shown. The lower panel shows example source localisation for both OPM (green) and SQUID (blue) systems). (Adapted from Feys et al. [49]).

**Figure 6.**

Physics of an OPM. A) A basic diagram showing the key components of a single axis OPM including the ^{87}Rb cell, laser beam, photodetector, and modulation coils (Adapted from Boto et al. [38]). B) A basic diagram showing the same components as in A but for a triaxial OPM. A beam splitter is used to produce the two beams laser beams. C) A schematic diagram of the atomic structure of ^{87}Rb and the transitions involved in optical pumping. D) The solution to the Bloch equations plotted as a function of B_x . In the y-direction the solution is a dispersion curve and in the z-direction the solution is a Lorentzian. E) The approximately linear response of the OPM shown between ± 5 nT.

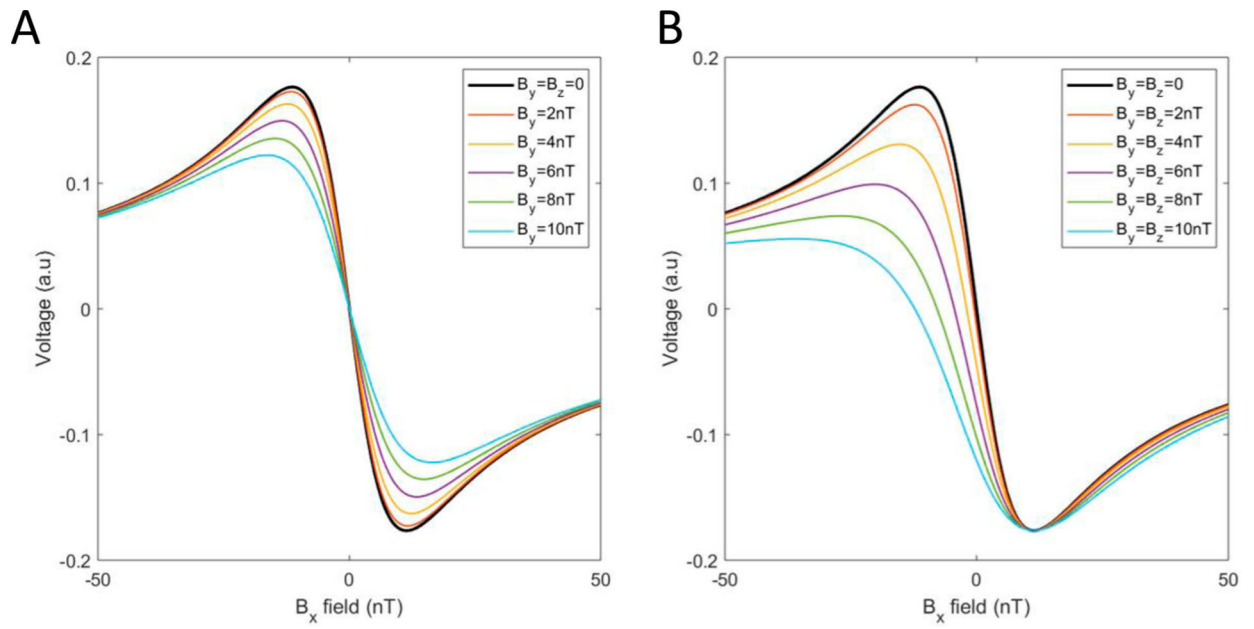


Figure 7.

The full solution to the Bloch equations plotted for the case where $B_y = B_z = 0$ is not valid.

A) The solution with non-zero values of B_y and B) non-zero values of B_y and B_z .

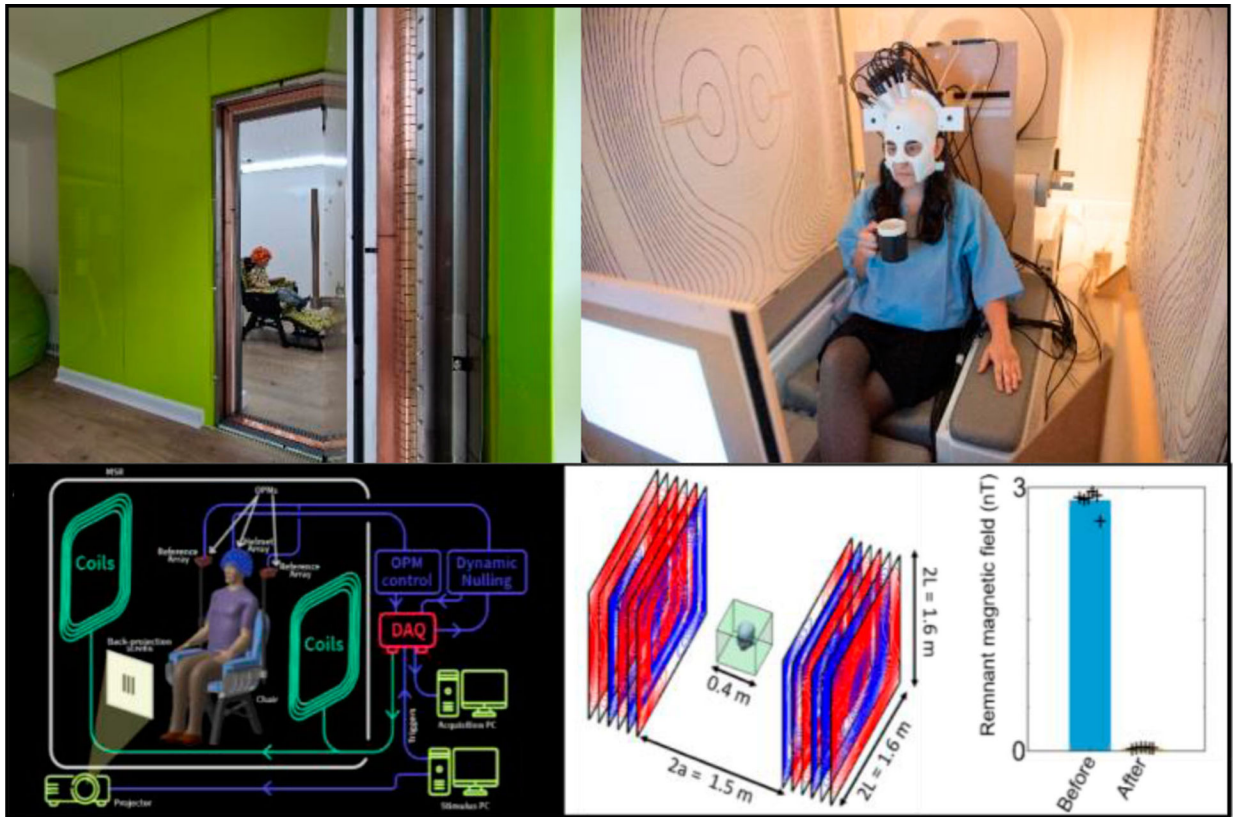


Figure 8.

Examples of shielding for OPM-MEG. A) A magnetically shielded room (built by Magnetic Shields Ltd) used for OPM-MEG at Young Epilepsy, UK. B) An early iteration of bi-planar coils (Holmes et al. [42]). C) A schematic diagram of a complete OPM-MEG system. C) Left: a schematic diagram of the fingerprint coil system used for active shielding. Right: example results (using the method developed in Rea et al. [45]); prior to the field nulling procedure, the remnant field in a (OPM optimised) shielded room was ~ 3 nT; following nulling it is reduced to 0.04 nT.